Research Square

Preprints are preliminary reports that have not undergone peer review.
They should not be considered conclusive, used to inform clinical practice,
or referenced by the media as validated information.

# Effects of Persistent Joints on the Strain Failure of the Roof and Floor around a Circular Opening

**Hongwei Deng**
Central South University
**Jun Shen**
245511035@csu.edu.cn
Central South University
**Jingbo Xu**
Central South University
**Yao Liu**
Jinggangshan University

**Research Article**

**Keywords:** sandstone, biaxial compression, acoustic emission, through-going filled fissure, RA-AF

**Posted Date:** August 14th, 2026

**DOI:** https://doi.org/10.21203/rs.3.rs-10484747/v1

**License:** This work is licensed under a Creative Commons Attribution 4.0 International License.
Read Full License

**Additional Declarations:** No competing interests reported.

# Effects of Persistent Joints on the Strain Failure of the Roof and Floor around a Circular Opening

Hongwei Deng [a],Jun Shen [a, *],Jingbo Xu [a],Yao Liu [b]
[a] *School of Resources and Safety Engineering, Central South University, Changsha 410083, China*
[b] *School of Architectural Engineering, Jinggangshan University, Ji'an 343009, China*
denghw208@126.com (H. Deng); 245511035@csu.edu.cn (J. S); xjb_csu2020@163.com*(J.X);
Liuyao0008@jgsu.edu.cn (Y.L)
* Corresponding author:245511035@csu.edu.cn(J. S)

**Abstract:** To investigate localized damage concentration and coalescence-induced instability of surrounding rock where fault fracture zones coexist with roadway excavations, a circular opening was used to represent a roadway or underground cavern, while a through-going filled fissure represented a fault fracture zone or filled weak structural plane. Biaxial compression tests under low lateral confinement were conducted on intact sandstone, sandstone with a single circular opening, and opening–fissure specimens with different fissure inclinations and filling thicknesses. Global deformation, local deformation at the opening roof and floor, and acoustic emission (AE) responses were monitored simultaneously. At a fissure inclination of 15°, increasing the filling thickness from 2 mm to 5 mm and 10 mm increased the peak strength from 43.16 MPa to 48.96 MPa, followed by a slight decrease to 47.90 MPa, while the peak axial deformation generally increased. At a filling thickness of 2 mm, increasing the fissure inclination from 10° to 15° and 20° reduced the peak strength from 53.47 MPa to 43.16 MPa and then increased it to 55.61 MPa, whereas the peak axial deformation first decreased and then increased markedly. These results indicate non-monotonic effects of both fissure inclination and filling thickness. Increasing the filling thickness intensified AE activity during the middle and late loading stages and markedly increased the proportion of shear-type events, which reached 67.5% and 63.9% for the 5 mm and 10 mm specimens, respectively. At a fissure inclination of 20°, the shear-event proportion increased to 21.0%, indicating a transition from tensile-dominated failure to tensile–shear mixed or shear-dominated failure. Considering peak strength, local deformation around the opening, and local instability time, specimen s-15-2 exhibited the strongest deformation concentration and earliest instability, indicating the poorest overall stability, whereas s-15-5 showed relatively high strength, the latest roof instability, and limited floor deformation, indicating comparatively better stability. These findings provide an experimental basis for instability assessment, hazardous-zone delineation, and support optimization for roadways adjacent to fault fracture zones.

**Keywords:** sandstone; biaxial compression; acoustic emission; through-going filled fissure; RA-AF

## 1. Introduction

With the progressive development of mineral resources toward greater depths, underground roadways, chambers, and stope surrounding rocks are increasingly subjected to complex stress environments. Natural rock masses commonly contain fissures, joints, weak interlayers, and other defects formed during long-term geological processes, while excavation and mining disturbances further modify the stress distribution in the vicinity of these defects. Under laboratory conditions, underground roadways and chambers can, to some extent, be idealized as circular openings within rock specimens, whereas fault fracture zones, filled joints, and weak interlayers can be represented by through-going filled fissures with specified inclination angles and thicknesses. When a circular opening and a filled fissure coexist, stress concentration around the opening interacts with the stiffness degradation induced by the fissure, thereby facilitating crack initiation, propagation, and coalescence and ultimately reducing the load-bearing capacity of the surrounding rock and increasing the risk of local instability. In a review of the fracture mechanical behavior of rocks containing various

defects, Zhao et al. (2023) noted that defect type, geometry, and spatial configuration are key factors governing strength degradation and fracture trajectories. Therefore, investigating the mechanical response and failure evolution of sandstone containing combined circular-hole and through-going filled-fissure defects under biaxial stress conditions is of considerable significance for the stability assessment and support design of rock masses containing complex defects.

Extensive studies have been conducted on the effects of holes and fissures on the mechanical behavior of rocks. Wong and Einstein (2009) systematically investigated crack initiation and propagation in specimens containing a single fissure and demonstrated that fissure inclination significantly affects the development of wing cracks, secondary cracks, and final coalescence patterns. Huang et al. (2016) found that the inclination angles of two nonparallel fissures and the geometry of the intervening rock bridge jointly control crack propagation paths and macroscopic failure modes. Yang et al. (2014) reported that combined fissures markedly reduce the load-bearing capacity of sandstone and that the spatial relationship between defects determines whether crack coalescence occurs within the rock-bridge region. For rocks containing openings, Zhu et al. (2015) found that the spacing and arrangement of two circular holes alter stress concentration within the inter-hole rock bridge and consequently modify crack linkage patterns. Yang et al. (2017) further demonstrated that the orientation of elliptical flaws and the rock-bridge angle exert pronounced nonlinear effects on the peak strength, deformation characteristics, and crack evolution of sandstone. Chen et al. (2017) conducted uniaxial compression tests on sandstone containing two fissures and a single circular hole and observed that cracks generally initiate from the hole boundary and fissure tips before propagating and coalescing through the rock bridges between the opening and fissures. Liu et al. (2019) and Yang et al. (2019) investigated sandstone containing elliptical hole–fissure defects and circular hole–nonpersistent joint defects, respectively, and both studies confirmed a significant coupling effect between stress concentration around the opening and the crack-driving effect at fissure tips. More recently, Dong et al. (2024) employed acoustic emission and deformation monitoring and found that hole–joint interaction changes the crack initiation angle, damage distribution, and dominant fracture path. These findings indicate that holes and fissures do not influence rock failure independently; rather, their spatial configuration and interaction play a decisive role in determining specimen strength and crack coalescence behavior.

Fissures in natural rock masses are rarely completely open and are commonly filled with clay, rock fragments, or cemented materials. Such filling materials alter the contact condition and load-transfer mechanism along the fissure, causing the mechanical behavior of filled-fissure rock masses to differ substantially from that of rocks containing open fissures. Through laboratory tests and extended finite-element simulations, Zhuang et al. (2014) found that fissure filling can increase the peak strength of specimens and alter the initiation time, location, and propagation path of cracks. Miao et al. (2018) investigated the fracture behavior of sandstone containing a single filled fissure and showed that the filling material and fissure inclination jointly control the transition among interface cracking, wing-crack propagation, and shear failure. Sharafisafa et al. (2019) demonstrated that the stiffness of the filling material and its bonding performance with the surrounding matrix determine the load-bearing capacity and crack-deflection behavior of defected specimens. Wang et al. (2019), through combined experimental and numerical analyses, reported that the inclination angles of two filled fissures and the geometry of the rock bridge significantly affect the equivalent shear strength and macroscopic failure mode. Le et al. (2021) found that grouting improves load transfer across fissured regions and reduces stress concentration at fissure tips. Su et al. (2025) further showed that the bonding and deformation compatibility of the grout–rock interface determine whether cracks penetrate the filling material or propagate preferentially along the interface. Under biaxial compression, Lei et al. (2020) investigated sandstone containing two parallel filled fissures and found that lateral confinement and fissure geometry jointly govern crack evolution and acoustic emission responses. However, previous studies have mainly focused on whether fissures are filled, the mechanical properties of the filling material, and fissure inclination, whereas the influence of filling thickness has received comparatively limited attention.

Rock masses in underground engineering are generally subjected to multiaxial stress states, and uniaxial compression tests cannot fully reproduce the actual failure behavior of combined hole–fissure defects under lateral

confinement. Du et al. (2021) reported that biaxial confinement alters the peak strength, deformation capacity, failure mode, and acoustic emission activity of rocks. Ji et al. (2024), using biaxial loading in combination with acoustic emission monitoring, digital image correlation, and three-dimensional imaging, demonstrated that lateral stress suppresses crack opening and changes the three-dimensional extent of damage in defected specimens. True-triaxial tests conducted by Zhang et al. (2023) and Li et al. (2026) showed that the intermediate principal stress modifies the spatial direction of crack propagation and increases the contribution of shear cracking to final failure. Peng et al. (2024) found that axial stress redistributes stress concentration around an opening and influences spalling and rockburst-like failure in deep roadways. Miao et al. (2025) showed that biaxial confinement significantly controls the yielding behavior and brittle-to-ductile transition of sandstone containing openings. B. Liu et al. (2025) investigated the effect of a single fissure on failure around a circular opening under biaxial compression and found that fissure orientation determines the crack coalescence path between the fissure and the opening. T. Liu et al. (2025) further examined red sandstone containing combined hole–fissure defects under biaxial compression and revealed a pronounced coupling effect among lateral stress, stress concentration around the opening, and fissure-induced weakening. These studies indicate that biaxial confinement not only restricts fissure opening and sliding but also modifies stress transfer between the opening and fissure; therefore, its effects cannot be directly inferred from uniaxial test results.

Acoustic emission technology can continuously record microcracking activity within rocks and is therefore an effective tool for investigating the progressive failure of defected rock masses. Liu et al. (2015) used acoustic emission moment tensor analysis to identify the spatial evolution of tensile and shear cracks around a circular opening. Ohno and Ohtsu (2010) proposed the use of RA and AF values to distinguish tensile cracking from shear cracking, thereby establishing a fundamental framework for fracture-mode identification. Niu et al. (2020) showed that the failure of flawed sandstone generally evolves from tensile-dominated cracking toward mixed tensile–shear failure as loading proceeds. Jiang et al. (2024) and Li et al. (2024) demonstrated that acoustic emission ring counts, energy, and other characteristic parameters can reflect the stages of crack closure, stable propagation, and unstable coalescence. Liu et al. (2022) revealed the transition of sandstone from stable damage accumulation to unstable failure from the perspectives of acoustic emission and energy evolution. Loading rate, cyclic loading, and complex stress paths also modify the temporal distribution of acoustic emission activity and the precursory characteristics of failure (Qin et al. 2018; Li et al. 2023; H. Wang et al. 2024; Zhou et al. 2024). Yu et al. (2024) and Zhao et al. (2024) further showed that abrupt increases in acoustic emission activity, together with localized strain concentration, can be used to identify crack localization and impending instability. To improve the objectivity of tensile–shear crack classification, J.X. Wang et al. (2024) employed the Kneedle algorithm to determine the dividing boundary in the RA–AF plane, whereas Xue et al. (2026) used a Gaussian mixture model to classify acoustic emission events in fissured sandstone with different inclination angles. Q. Liu et al. (2025) and Zhao et al. (2026) also developed acoustic-emission-based damage characterization approaches, confirming that acoustic emission parameters can effectively describe damage accumulation and the evolution of fracture modes in flawed sandstone.

In summary, previous studies have clarified the fundamental failure behavior of defected rocks from the perspectives of hole geometry, fissure inclination, defect configuration, filling material, stress path, and acoustic emission response. Nevertheless, several issues remain unresolved. First, most existing studies have focused on open or nonpersistent fissures, and the mechanical behavior of sandstone containing both a circular hole and a through-going filled fissure remains insufficiently understood. Second, studies on filled fissures have mainly considered the type of filling material and fissure inclination, whereas systematic comparisons of the independent effects of filling thickness and low fissure inclination under otherwise identical biaxial boundary conditions remain limited. Third, most experiments have been conducted under uniaxial compression, and the coupling mechanism among stress concentration around the opening, weakening induced by the filled fissure, and deformation incompatibility at the filling–rock interface under biaxial confinement has not yet been fully clarified. In addition, a comprehensive relationship among macroscopic

stress–strain response, local deformation, acoustic emission activity, tensile–shear crack evolution, and final failure pattern has yet to be established.

Accordingly, this study investigates the mechanical response and failure evolution of sandstone specimens containing a circular opening and a through-going filled fissure under low lateral confinement. Two one-factor test series are considered: fissure inclinations of 10°, 15°, and 20° at a constant filling thickness of 2 mm, and filling thicknesses of 2, 5, and 10 mm at a constant inclination of 15°. Intact and single-opening specimens are used as reference groups. Axial displacement, local deformation at the opening roof and floor, AE ring-down counts, and RA–AF parameters are analyzed to identify changes in load-bearing behavior, deformation localization, and AE-source type. The macroscopic failure patterns are further compared with the AE results to clarify the coupled influence of opening-induced stress concentration and the through-going filled discontinuity.

## 2. Experimental Method

### 2.1 Specimen preparation

The sandstone used in the tests was collected from a quarry in Liuyang, Hunan Province, and all specimens were taken from the same fresh, unweathered rock block. According to the recommended methods of the International Society for Rock Mechanics (ISRM), the rock was processed into cubic specimens of 100 mm x 100 mm x 100 mm. A 10 mm diameter through-going circular hole was then drilled at the specimen center using a water-drilling method. The specimens were cut according to the preset fissure inclination and filled-fissure thickness. After cutting, a cementitious filling material was used to bond the cut surfaces, thereby forming a through-going filled fissure. To reduce the influence of preparation differences on the test results, the fissure contact surfaces of all specimens were cleaned after cutting, and the filling layers were prepared using the same mix proportion, curing time, and environmental conditions. The prepared specimens are shown in Fig. 1.

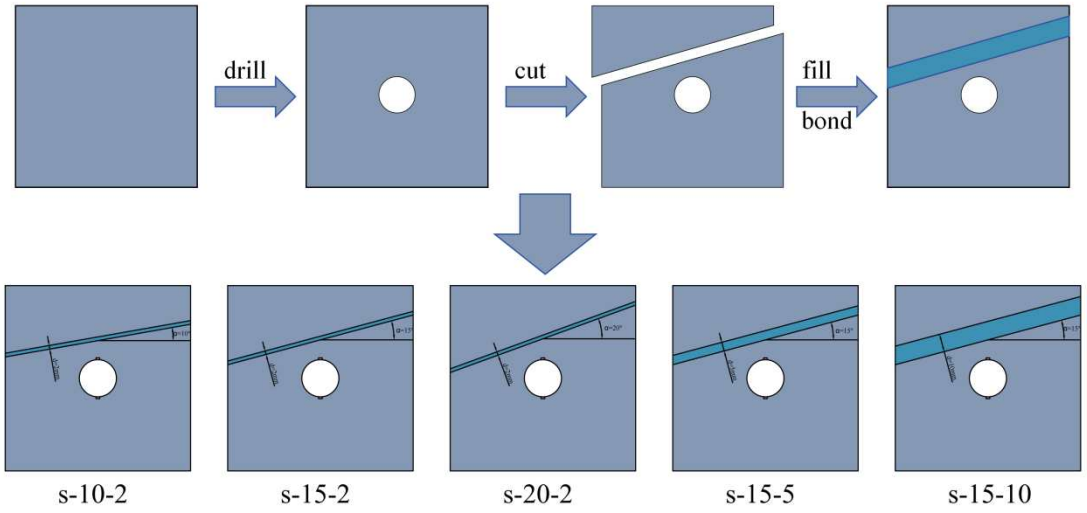



**Fig. 1 Sandstone specimen containing a circular hole and a through-going filled fissure**

To investigate the effects of fissure inclination and filled-fissure thickness on the mechanical response and AE characteristics of sandstone containing a hole, two single-factor test series were designed. In the first series, the filling thickness was kept constant at 2 mm, while the fissure inclinations were set to 10°, 15°, and 20°. In the second series, the fissure inclination was kept constant at 15°, while the filled-fissure thicknesses were set to 2 mm, 5 mm, and 10 mm. The specimen ID follows the form “s-α-d”, where “s” denotes sandstone, “α” denotes fissure inclination, and “d” denotes filled-fissure thickness. For example, s-10-2 represents a sandstone specimen with a fissure inclination of 10° and a filled-fissure thickness of 2 mm. Specimen s-15-2 is used as the common reference condition for both the inclination-effect and thickness-effect series.

The three typical filled-fissure thicknesses of 2 mm, 5 mm, and 10 mm were selected to simulate weak filled

interlayers with different widths in engineering rock masses while considering the specimen size effect and preparation stability. Specifically, 2 mm represents a thin filled weak plane, 5 mm represents a medium-thickness weak interlayer, and 10 mm represents a relatively thick weak interlayer. These different thicknesses correspond to different degrees of structural weakening and can be used to analyze the effect of weak-interlayer width on the mechanical response, AE characteristics, and crack evolution behavior of the specimens.

Layered structural planes, argillaceous interlayers, and sedimentary weak planes in engineering rock masses are often nearly horizontal or have low inclinations. Under lateral confinement, they are prone to compression-shear coupled instability. Therefore, this study focuses on the influence of through-going filled fissures with low inclinations of 10°-20° on the failure behavior of sandstone containing a circular hole.

To obtain the basic mechanical parameters of the sandstone matrix and filling material, compression, tensile, and shear tests were conducted on red sandstone and the cementitious filling material. The test results are listed in Table 1. These parameters are used to characterize the mechanical contrast between the rock matrix and the filled weak interlayer and provide a basis for the subsequent failure-mechanism analysis.

**Table 1 Basic Rock Mechanical Properties of Experimental Materials**

| Material Name | | Red Sandstone | Cementitious filling material |
|---|---|---|---|
| Density（ρ）/kg·m⁻³ | | $2.98\times10^3$ | $1.45\times10^3$ |
| Compressive Properties | Compressive Strength/MPa | 35.47 | 7.54 |
| | Elastic Modulus（E）/GPa | 14.37 | 3.65 |
| | Poisson's Ratio（ν） | 0.24 | 0.38 |
| Shear Properties | Cohesion（c）/MPa | 16.73 | 4.86 |
| | Internal Friction Angle（φ）/° | 38.4 | 43.2 |
| Tensile Properties | Tensile Strength /MPa | 2.44 | 1.02 |

## 2.2 Test scheme

To prevent premature sliding instability along the structural plane in the initial loading stage of filled-fissure specimens, a low lateral confining stress was applied during the tests. This was intended to simulate the lateral confinement experienced by surrounding rock in underground engineering and to highlight the crack propagation and failure evolution characteristics of hole-through-going filled fissure combined defects under compression.

Biaxial compression tests and AE monitoring were conducted on intact sandstone specimens, single-hole sandstone specimens, and sandstone specimens containing a circular hole and through-going filled fissures with different inclinations and filling thicknesses. Strain gauges were arranged above and below the central hole to monitor the local deformation evolution around the hole. The loading equipment was a rock true-triaxial electro-hydraulic servo-induced disturbance test system jointly developed by Central South University and Changchun Chaoyang Testing Instrument Co., Ltd. The system can independently load the X, Y, and Z directions. The maximum loading capacities in the X and Y directions are 2000 kN, and that in the Z direction is 3000 kN. The loading rate ranges from 10^1 to 10^4 N/s. AE monitoring was performed using a PCI-2 acoustic emission acquisition system, with a preamplifier gain of 40 dB, a threshold of 40 dB, and a sampling rate of 5 MSPS.

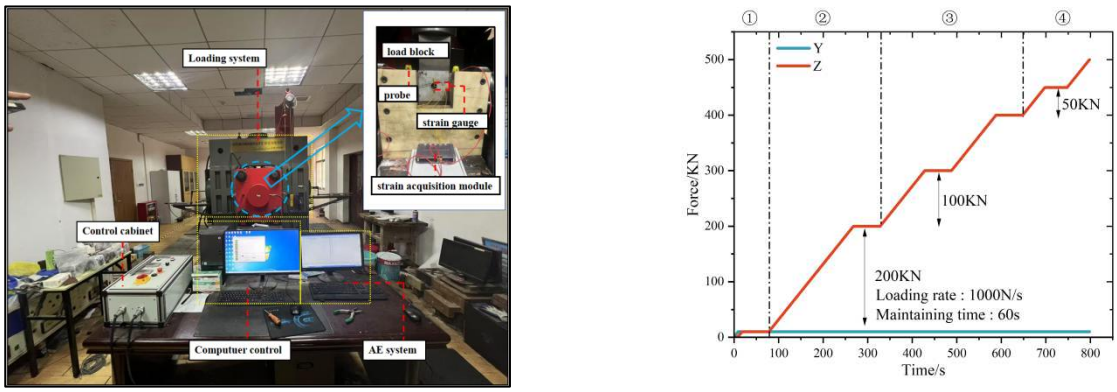
**Table 2 Acoustic Emission Monitoring Parameters**

| Sensor number | Preamplifier Gain | Sampling rate | Threshold | Sample length | Resonant frequency |
|---|---|---|---|---|---|
| 2 | 40 dB | 5 MSPS | 40 dB | 3 K | 150 KHz |

The test procedure was as follows. Before testing, the specimen end surfaces were ground with sandpaper to ensure flat loading surfaces and improve loading uniformity. A thin layer of Vaseline was then uniformly applied to the specimen end surfaces to reduce the effect of end friction on the test results. Before installing the AE probes, a small amount of coupling agent was applied to the probe contact surfaces to improve the coupling between the probes and the loading

blocks and to ensure the accuracy and stability of AE signal acquisition. After specimen installation, the loads in the Y and Z directions were first adjusted to 1 kN to fix the specimen initially and ensure full contact with the loading end surfaces. After the specimen state became stable, the loading system and AE monitoring system were started to record the mechanical response and AE signals during loading and failure in real time.

Force-controlled loading was adopted at a rate of 1 kN/s. After specimen installation, the Y- and Z-direction loads were first preloaded to 1 kN to ensure sufficient contact at the loading surfaces. The Y-direction load was then increased to 10 kN and maintained approximately constant during subsequent loading to simulate low lateral confinement. The Z-direction load was then increased to 10 kN and held for 1 min. Based on the original cross-sectional area of 100 mm x 100 mm, a 10 kN load corresponds to a nominal stress of approximately 1 MPa. Thereafter, staged loading was continued in the Z direction to 200 kN, 300 kN, and 400 kN successively, with each loading level held for 1 min. After the Z-direction load reached 400 kN, it was increased in increments of 50 kN until specimen instability and failure occurred. The test system and loading path are shown in Fig. 2.




（a）Experimental System　　（b）Loading Curve

**Fig. 2 Experimental System and Loading Curve**

## 3. Test Results and Discussion

### 3.1 Stress-strain curve analysis

The stress-strain curve directly reflects the load-bearing capacity and deformation response of a specimen during loading. For sandstone containing a circular hole and a through-going filled fissure, the hole changes the internal continuous load-bearing structure, while the filled fissure further affects the load transfer path. Therefore, it is necessary to first compare the overall mechanical responses of specimens with different defect configurations using stress-strain curves. The stress-strain curves of different specimens are shown in Fig. 3.

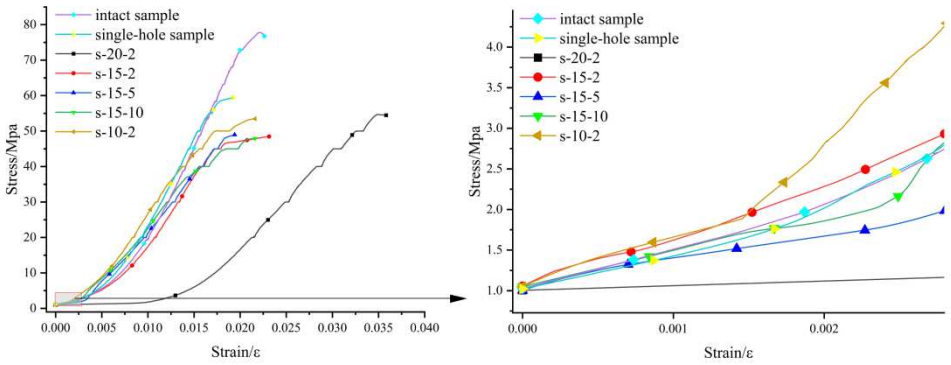



**Fig. 3 Stress–strain curves of specimens**

As shown in Fig. 3, the stress-strain curves of all specimens generally increase with increasing strain, but the curve slope, peak strength, and peak strain differ significantly. The intact specimen shows a rapid increase in the curve and the

highest overall load-bearing capacity. The single-hole specimen exhibits a clear decrease in strength, indicating that the hole weakens the load-bearing structure of the specimen. After a through-going filled fissure is introduced, the curves of the specimens generally shift downward, and the peak strengths are lower than that of the single-hole specimen, indicating an additional influence of the fissure structure on the mechanical response of sandstone containing a hole.

Among the fissured specimens, the s-20-2 curve is distinctive. Its initial slope is relatively small, the peak strain is clearly larger, and the pre-peak deformation process is more fully developed. Specimen s-15-2 has the lowest peak strength and an overall lower curve level, showing a more pronounced weakening of load-bearing capacity. Specimen s-10-2 increases more rapidly during the initial stage, but its peak appears relatively early.

When the fissure inclination is fixed at 15°, the peak strength first increases and then decreases slightly as the filled-fissure thickness increases. In terms of curve shape, s-15-2 has a steep rising segment but reaches the peak relatively early, with a smaller peak strain. The peaks of s-15-5 and s-15-10 are delayed, and their pre-peak deformation processes are prolonged. Overall, the filled-fissure thickness has a regulating effect on curve shape and peak strain, but the variation is not monotonic within the tested range.

These variations are related to the mechanical differences between the filling material and the sandstone matrix. The strength and stiffness of the filling material are lower than those of the sandstone matrix, and the presence of the through-going filled fissure changes the continuous load-bearing path of the specimen. Under a thin filling layer, the weak plane exerts a more direct weakening effect on load-bearing capacity. As the thickness increases, compaction deformation of the filling layer has a stronger regulating effect on the overall deformation process. However, when the proportion of weak material continues to increase, the load-bearing capacity decreases to some extent.

When the filled-fissure thickness is fixed at 2 mm, the peak strength first decreases and then increases as the fissure inclination increases from 10° to 15° and then to 20°. In terms of curve slope, s-10-2 increases rapidly in the initial stage, s-20-2 increases more slowly but has the largest peak strain, and s-15-2 remains at the lowest overall stress level. This suggests that fissure inclination affects the initial stiffness, peak strain, and overall load-bearing level, and the effect is not monotonic in the range considered in this study.

Changing the fissure inclination modifies the relative roles of normal compaction and tangential sliding along the filled fissure plane and also affects the spatial relationship between the hole and the fissure. These factors lead to differences in the pre-peak deformation process and peak response among the specimens.

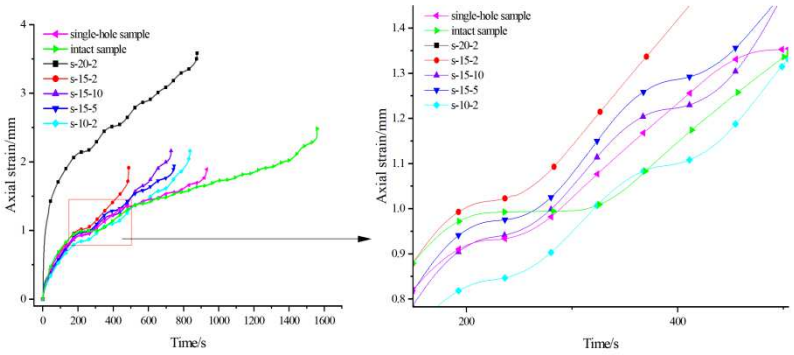



**Fig. 4 Axial strain–time curves of specimens**

As shown in Fig. 4, the pre-peak axial deformation differs among the specimens. The intact specimen undergoes a relatively large pre-peak axial deformation, indicating a more sufficient deformation accumulation process before reaching the peak strength. The pre-peak axial deformation of the single-hole specimen is smaller than that of the intact specimen, indicating that the hole defect causes the specimen to enter the failure stage earlier.

For specimens containing both a hole and a through-going filled fissure, the pre-peak axial deformations of s-15-2 and s-15-5 are close to that of the single-hole specimen, indicating little change in overall deformability. The pre-peak axial

deformations of s-15-10 and s-10-2 increase to some extent, suggesting a certain deformation accumulation process before the peak. Specimen s-20-2 exhibits the largest pre-peak axial deformation, indicating more pronounced deformation development before peak strength under this condition. Overall, fissure inclination and filling thickness affect not only peak strength but also the pre-peak deformation process.

To compare more intuitively the influence of different defect configurations on load-bearing capacity, the peak strengths of different specimens were statistically analyzed based on the preceding stress-strain and deformation curves, as shown in Fig. 5.

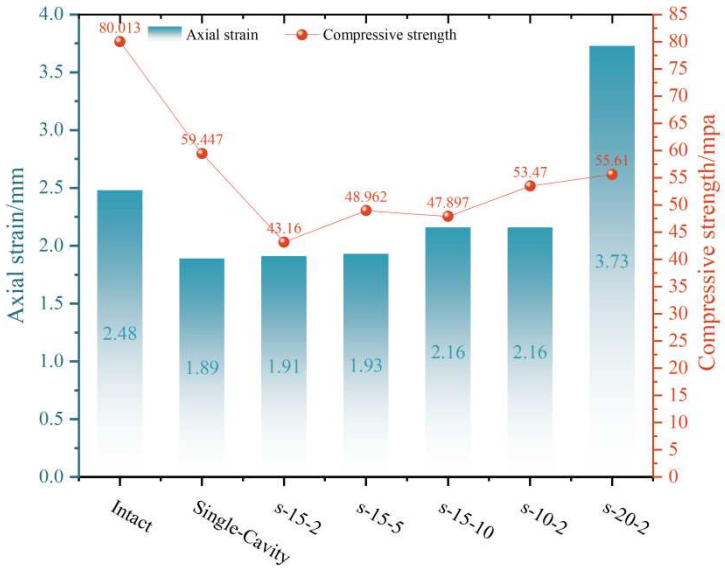



**Fig. 5 Peak strength and peak axial deformation of different specimens**

As shown in Fig. 5, the intact specimen has the highest peak strength and peak axial deformation, which are 80.13 MPa and 2.48 mm, respectively. For the single-hole specimen, the corresponding values decrease to 59.47 MPa and 1.89 mm. Compared with the single-hole specimen, the intact specimen shows increases of 34.75% in peak strength and 31.22% in peak axial deformation. This indicates that the introduction of a hole markedly weakens the load-bearing capacity of the specimen and causes it to enter the peak stage at a lower deformation level.

The peak strengths of all specimens containing both a hole and a through-going filled fissure are lower than that of the single-hole specimen, while their peak axial deformations generally increase. The peak strengths of s-15-2, s-15-5, s-15-10, s-10-2, and s-20-2 are lower than that of the single-hole specimen by 27.43%, 17.67%, 19.46%, 10.09%, and 6.51%, respectively. Their peak axial deformations increase by 1.06%, 2.12%, 14.29%, 14.29%, and 97.35%, respectively. Thus, the through-going filled fissure further reduces the strength of the hole-containing specimen, but the changes in peak axial deformation vary substantially among different conditions; in particular, s-20-2 shows the most pronounced increase.

When the fissure inclination is fixed at 15°, increasing the filled-fissure thickness from 2 mm to 5 mm raises the peak strength from 43.16 MPa to 48.96 MPa, reducing the strength loss relative to the single-hole specimen from 27.43% to 17.67%. When the thickness is further increased to 10 mm, the peak strength decreases slightly to 47.90 MPa, corresponding to a 19.46% reduction relative to the single-hole specimen. Meanwhile, the peak axial deformation increases from 1.91 mm and 1.93 mm to 2.16 mm, corresponding to increases of 1.06%, 2.12%, and 14.29% relative to the single-hole specimen. This indicates that under a 15° inclination, increasing the filling thickness generally increases the peak axial deformation, while the peak strength first increases and then decreases slightly.

When the filled-fissure thickness is fixed at 2 mm, increasing the fissure inclination from 10° to 15° decreases the peak strength from 53.47 MPa to 43.16 MPa, and the strength reduction relative to the single-hole specimen increases from 10.09% to 27.43%. When the inclination is further increased to 20°, the peak strength rises to 55.61 MPa, only 6.51% lower

than that of the single-hole specimen. The peak axial deformation decreases from 2.16 mm to 1.91 mm and then increases to 3.73 mm, corresponding to increases of 14.29%, 1.06%, and 97.35%, respectively, relative to the single-hole specimen. Therefore, under a 2 mm filling thickness, the effects of fissure inclination on strength and peak axial deformation are both non-monotonic within the tested range. Specimen s-15-2 shows the most pronounced strength weakening, while s-20-2 has the largest peak axial deformation.

Overall, the circular hole and through-going filled fissure jointly reduce the peak strength of the specimens, whereas the peak axial deformation does not decrease synchronously. This behavior is related to the weakening of the load-bearing cross section caused by the hole, stress concentration around the hole, and the structural discontinuity induced by the filled fissure. The fissure thickness and inclination change the internal load transfer and deformation coordination process, resulting in differentiated peak strength and peak axial deformation responses under different conditions.

### 3.2 Temporal evolution of local deformation at the cavity roof and floor

To further analyze the temporal evolution of local deformation at different locations around the hole, the roof and floor areas of the hole were selected as monitoring points. The strain-gauge measurements were converted into local deformation values to obtain the time-dependent evolution curves, as shown in Fig. 6. The roof monitoring point characterizes the local deformation response of the upper compressed area around the hole, while the floor monitoring point reflects the deformation adjustment behavior of the lower area during load transfer. By comparing the local deformation evolution of the two monitoring points under biaxial compression, the influence of the through-going filled fissure and hole combined defects on the deformation distribution around the hole can be further revealed. The local deformation evolution curves at the cavity roof and floor are shown in Figs. 7 and 8, respectively.

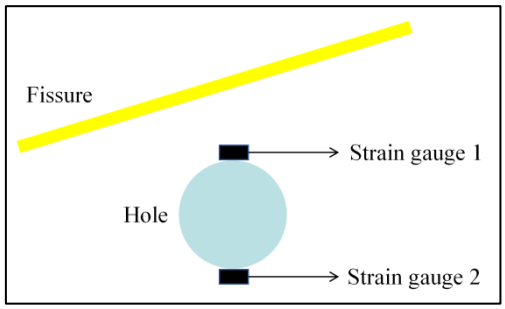



**Fig. 6 Local deformation monitoring positions**

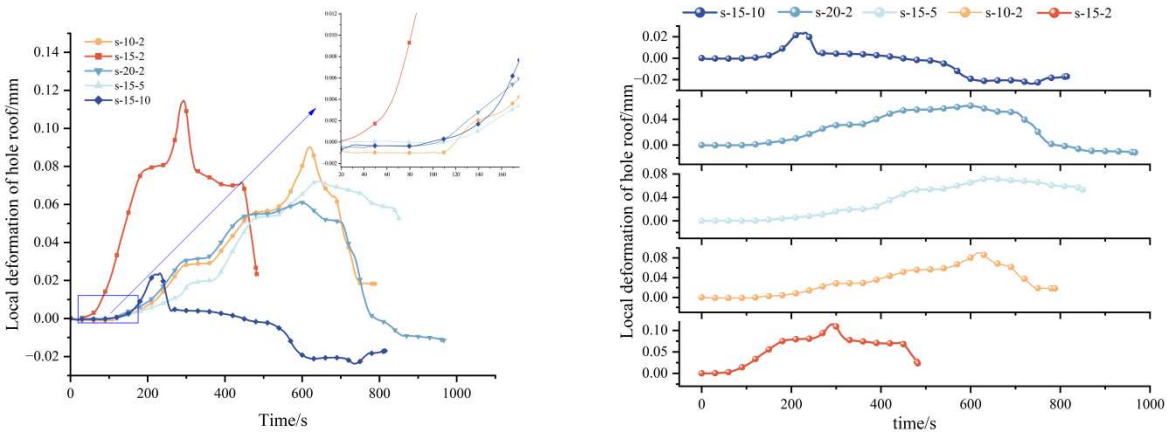



**Fig. 7 Evolution of local deformation at the cavity roof under different filled fissure parameters**

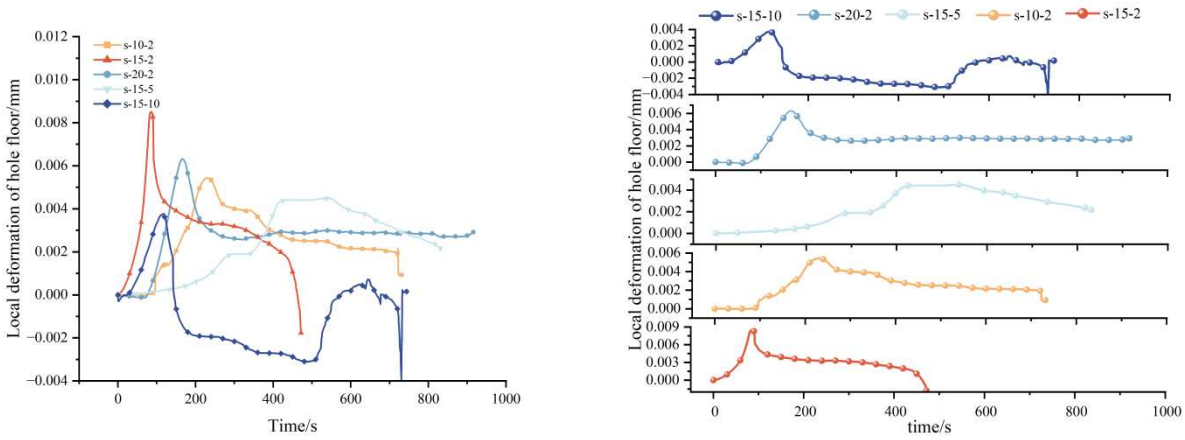



**Fig. 8 Evolution of local deformation at the cavity floor under different filled fissure parameters**

As shown in Figs. 7 and 8, the local deformation curves at the cavity roof and floor of different specimens exhibit certain stage characteristics, but the deformation peaks and evolution processes differ markedly. Overall, the peak local deformation at the cavity roof is significantly larger than that at the floor. The floor curves have smaller overall amplitudes, and some specimens show fluctuations or reverse changes during loading, indicating asynchronous local deformation between the upper and lower parts of the hole.

Figure 7 shows that the local deformation at the cavity roof is generally small in the early loading stage and gradually becomes differentiated with increasing loading time. The roof deformation of s-15-2 increases most significantly, reaching a relatively high peak at approximately 300 s before decreasing. The roof deformation of s-10-2 and s-15-5 gradually increases in the middle-to-late stage, and their peaks occur relatively late. The roof deformation amplitude of s-20-2 is at an intermediate level. The s-15-10 specimen shows the smallest roof deformation amplitude, but its curve changes markedly in the later stage. These results indicate that the local deformation development process at the cavity roof differs under different fissure inclination and filling thickness conditions.

Figure 8 shows that the floor deformation peak of s-15-2 is relatively high but decreases rapidly after reaching the peak. The floor deformation of s-20-2 and s-10-2 reaches a peak in the middle stage and then tends to become stable or decrease. The floor deformation of s-15-5 increases slowly and reaches its peak relatively late. The floor deformation of s-15-10 has a small amplitude and shows positive and negative changes. Compared with the roof, differences in the floor curves are mainly manifested as local fluctuations and stagewise adjustments.

To quantitatively compare local deformation differences at the roof and floor of the hole, the peak local deformation, time to peak, and local instability time were extracted from each curve. The results are listed in Table 3.

**Table 3 Statistical Results of Characteristic Parameters**

| Position | Specimen ID | Peak local deformation (mm) | Time to peak (s) | Local instability time (s) |
|---|---|---|---|---|
| Roof | s-10-2 | 0.09016 | 617.627 | 748.503 |
| | s-15-2 | 0.11463 | 294.747 | 447.745 |
| | s-20-2 | 0.06113 | 596.988 | 705.382 |
| | s-15-5 | 0.07205 | 635.631 | 834.003 |
| | s-15-10 | 0.02374 | 228.377 | 546.008 |
| Floor | s-10-2 | 0.0054 | 229.888 | 720.390 |
| | s-15-2 | 0.0085 | 85.895 | 427.897 |
| | s-20-2 | 0.0063 | 169.122 | 904.129 |
| | s-15-5 | 0.0044 | 411.562 | 537.357 |

| | | | | |
|---|---|---|---|---|
| | s-15-10 | 0.0038 | 114.386 | 510.007 |

Table 3 shows that the peak local deformation, peak-reaching time, and local instability time of the cavity roof and floor differ markedly among the specimens, indicating that fissure inclination and filled-fissure thickness affect the temporal evolution of local deformation around the hole. Some curves decrease or fluctuate after reaching the peak, suggesting a change in the local deformation state near the monitoring point, which may be associated with local unloading, stress redistribution, or crack development near the measuring point.

For the cavity roof, s-15-2 has the largest peak deformation of 0.11463 mm, followed by s-10-2 with 0.09016 mm. The peak values of s-15-5 and s-20-2 are 0.07205 mm and 0.06113 mm, respectively, while s-15-10 has the smallest value of 0.02374 mm. The descending order of roof peak local deformation is s-15-2 > s-10-2 > s-15-5 > s-20-2 > s-15-10. This indicates that the roof area of s-15-2 experiences the most pronounced local deformation, whereas s-15-10 shows the smallest deformation amplitude.

In terms of the peak-reaching time for roof local deformation, s-15-10 reaches the peak earliest at 228.377 s, followed by s-15-2 at 294.747 s. The peak-reaching times of s-20-2, s-10-2, and s-15-5 are 596.988 s, 617.627 s, and 635.631 s, respectively. Although s-15-10 reaches the peak early, its peak deformation is the smallest, indicating limited roof deformation amplitude. The s-15-5 specimen reaches the peak latest, suggesting delayed development of roof local deformation. In terms of roof local instability time, s-15-2 is the earliest at 447.745 s, followed by s-15-10 at 546.008 s; s-20-2 and s-10-2 occur at 705.382 s and 748.503 s, respectively, and s-15-5 is the latest at 834.003 s. This indicates that the roof area of s-15-2 enters local instability relatively early, whereas s-15-5 maintains roof local deformation for a longer time.

Further comparison of the interval between the peak time and local instability time of the roof shows that s-15-10 has the longest interval of 317.631 s, followed by s-15-5 with 198.372 s, s-15-2 with 152.998 s, s-10-2 with 130.876 s, and s-20-2 with the shortest interval of 108.394 s. This interval can characterize the duration from peak local deformation to local instability. The short post-peak duration of s-20-2 indicates that it enters local instability rapidly after reaching the peak. Although s-15-10 has the longest post-peak duration, its peak local deformation is low, and thus both peak magnitude and duration should be considered in evaluating the local deformation characteristics.

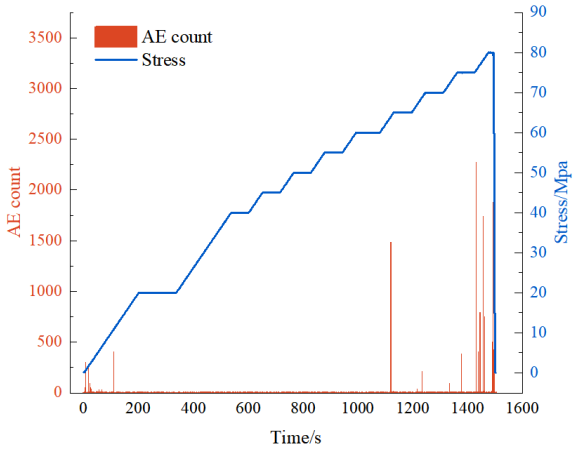
For the cavity floor, the peak local deformations are all much smaller than those at the roof. In descending order, the floor peak local deformation values are 0.0085 mm for s-15-2, 0.0063 mm for s-20-2, 0.0054 mm for s-10-2, 0.0044 mm for s-15-5, and 0.0038 mm for s-15-10. Similar to the roof results, s-15-2 still exhibits the largest floor peak deformation, indicating relatively pronounced local deformation at both the upper and lower parts of the hole. The s-15-10 specimen has the lowest floor peak deformation, consistent with its relatively low roof deformation.

In terms of the time to peak floor deformation, s-15-2 is the earliest at 85.895 s, followed by s-15-10 at 114.386 s, s-20-2 at 169.122 s, s-10-2 at 229.888 s, and s-15-5 at 411.562 s. Compared with the roof, the floor generally reaches its peak earlier, indicating that the floor area responds locally in the early loading stage but with smaller deformation amplitude. In terms of the floor local instability time, s-15-2 is the earliest at 427.897 s, followed by s-15-10 at 510.007 s, s-15-5 at 537.357 s, s-10-2 at 720.390 s, and s-20-2 at 904.129 s. The differences in floor local instability time indicate that the floor deformation process is also affected by fissure inclination and filling thickness.

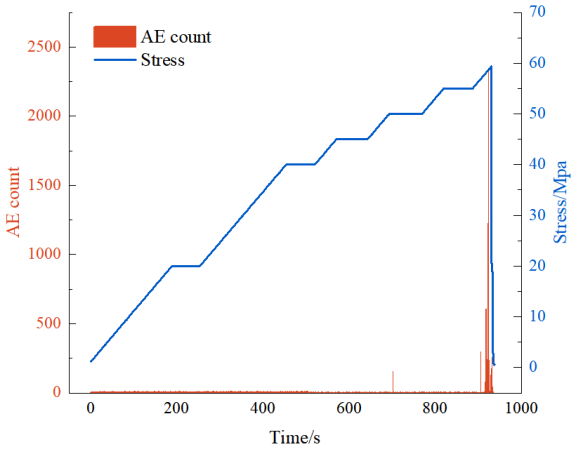
Taken together, the roof and floor results indicate clear spatial differences in local deformation around the hole. The peak deformation at the roof is generally larger than that at the floor, showing that the roof area is more sensitive to loading under the present conditions. Although the floor deformation amplitude is smaller, its peak generally occurs earlier, indicating an early local response. Among the different conditions, s-15-2 exhibits the largest peak local deformation at both the roof and floor and the earliest local instability time at both locations, implying the strongest local deformation concentration around the hole and relatively poorer stability. By contrast, s-15-5 has a higher peak strength than s-15-2, the latest roof local instability time, and a relatively small floor peak deformation, indicating a relatively gentle local deformation process under the present test conditions.

### 3.3 Evolution of AE ringing counts

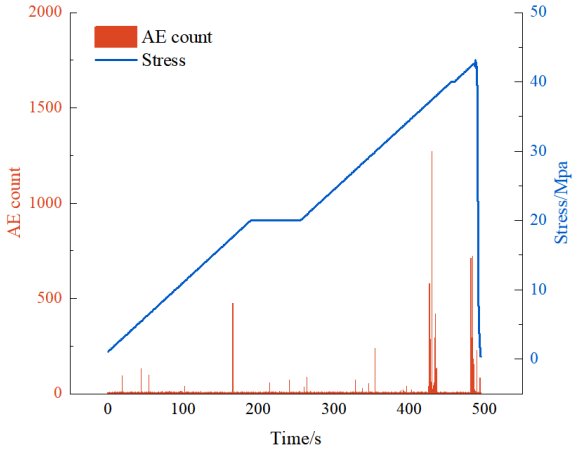
Figures 9 and 10 show the stress-AE ringing count curves and cumulative ringing count curves for the thickness-effect series and inclination-effect series, respectively. In Fig. 9, the fissure inclination is fixed at alpha = 15°, and the specimens include the intact specimen, single-hole specimen, s-15-2, s-15-5, and s-15-10. In Fig. 10, the fissure thickness is fixed at w = 2 mm, and the specimens include the intact specimen, single-hole specimen, s-10-2, s-15-2, and s-20-2. Comparisons of these two single-factor series reveal the effects of filled-fissure thickness and inclination on AE activity.



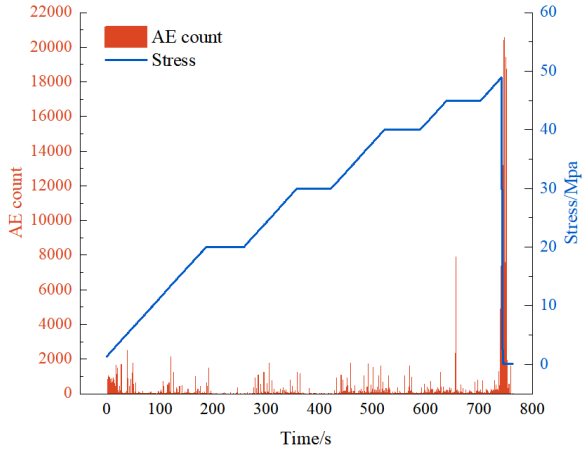

(a) intact specimen



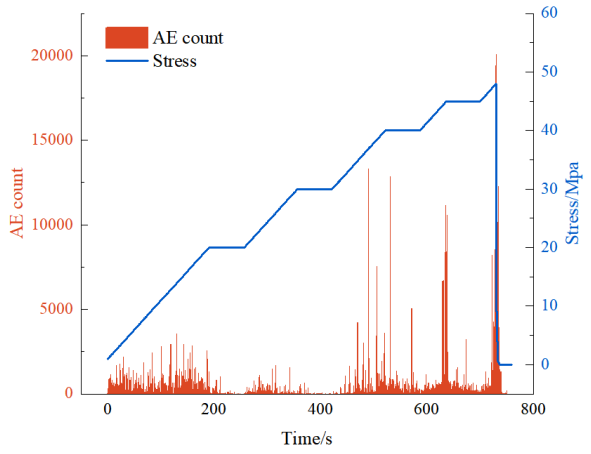

(b) single-hole specimen



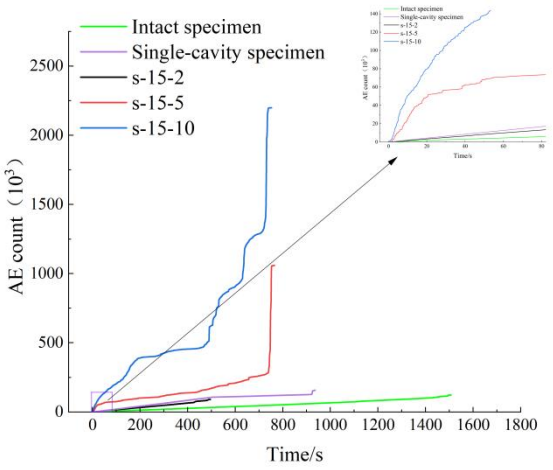

(c) s-15-2




(d) s-15-5

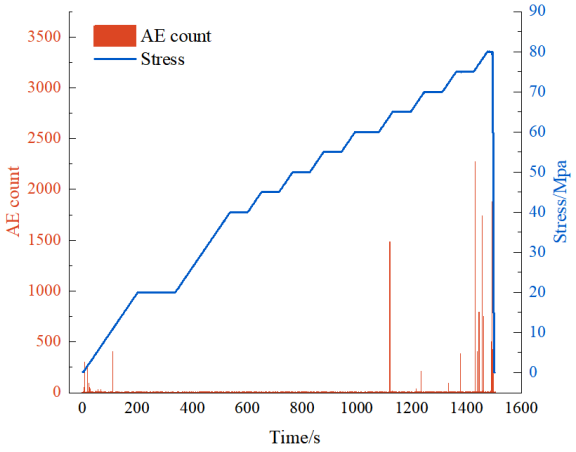



(e) s-15-10

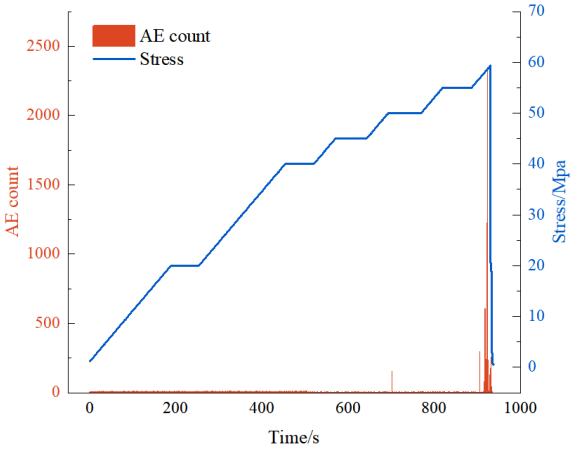



(f) Cumulative Ringing Count Curve

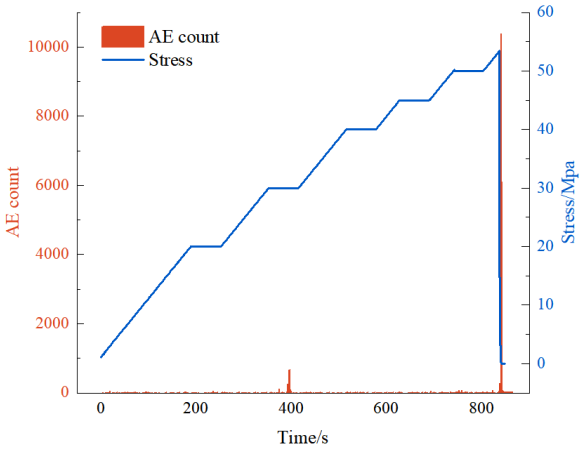
**Fig. 9 AE Ringing Count and Stress Loading Curves of Specimens with Different Weak Interlayer Thicknesses**



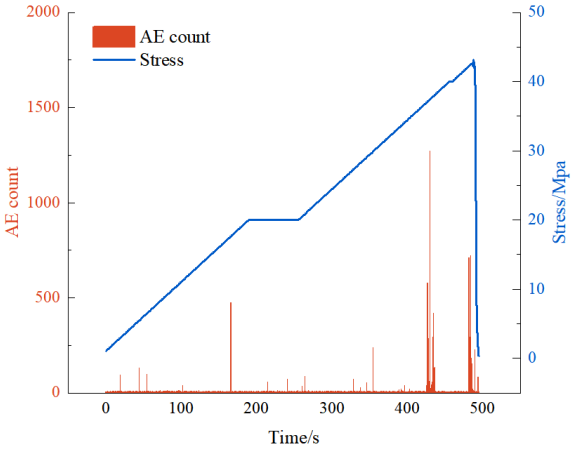

(a) intact specimen



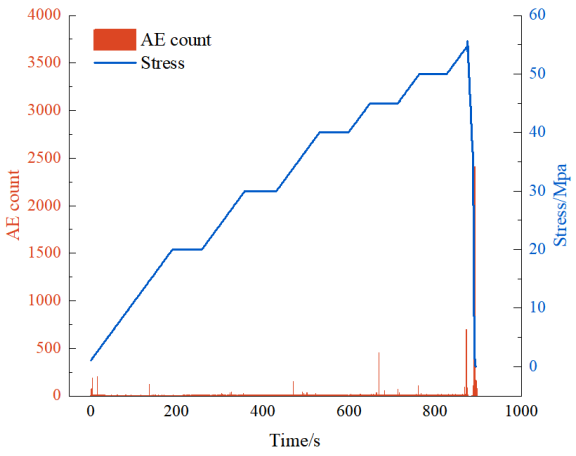

(b) single-hole specimen



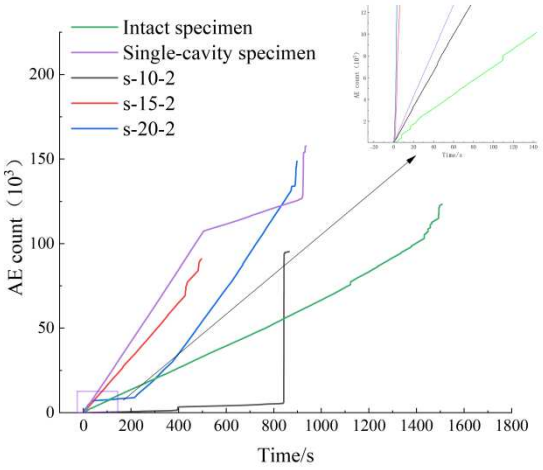

(c) s-10-2




(d) s-15-2




(e) s-20-2




(f) Cumulative Ringing Count Curve

**Fig. 10 AE Ringing Count and Stress Loading Curves of Specimens with Different Weak Interlayer Inclinations**

Overall, the AE ringing count evolution of each specimen exhibits clear stage characteristics. For the intact specimen, AE signals are scarce from the initial to middle loading stages, indicating that the specimen mainly undergoes closure of pre-existing microdefects and elastic deformation, with limited internal damage accumulation. Near the peak stress, AE ringing counts increase rapidly, and the slope of the cumulative ringing count curve rises markedly, indicating that microcracks enter a stage of rapid propagation and coalescence. For the single-hole specimen, the central hole changes the local stress distribution, and microcracks are more easily initiated near the hole edge due to stress concentration. However, its AE-active stage still mainly occurs in the late loading period, suggesting that a single hole changes the crack initiation position but does not fundamentally alter the overall feature of concentrated pre-peak failure.

As shown in Fig. 9, when the fissure inclination is kept constant at alpha = 15°, the AE activity of the specimens containing through-going filled fissures changes markedly with fissure thickness. The s-15-2 specimen exhibits relatively weak AE activity during most loading stages, and its cumulative ringing count increases slowly, indicating that internal damage under the thin filled fissure condition is mainly concentrated near failure. As the filled-fissure thickness increases to 5 mm and 10 mm, AE ringing counts increase significantly in the middle-to-late loading stage, and the slope of the cumulative ringing count curve becomes larger. This indicates that a thicker filling layer enhances sustained internal damage activity and makes crack initiation and propagation more developed. The reason is that as the filling layer becomes thicker, the range of the low-strength and low-stiffness weak interlayer increases, the continuous load transfer capacity of the sandstone matrix decreases, and deformation incompatibility, debonding, and frictional sliding at the rock-filling interface become more pronounced. These factors promote earlier AE events and concentrated release before instability.

It should be noted that the enhancement of AE activity caused by increased fissure thickness is not fully synchronized with the variation in peak strength. The stress-strain analysis indicates that the peak strengths of s-15-5 and s-15-10 are close to each other and both higher than that of s-15-2, whereas the AE results show more active internal damage in s-15-5 and s-15-10. This suggests that peak strength reflects only the load-bearing capacity when the specimen reaches global instability, whereas AE ringing counts can reveal crack propagation, interfacial sliding, and local damage accumulation before and after the peak. Therefore, for specimens containing filled weak interlayers, strength indices, local deformation, and AE responses should be considered together when interpreting the failure mechanism.

As shown in Fig. 10, when the fissure thickness is kept constant at w = 2 mm, fissure inclination affects the occurrence timing and cumulative release of AE events. The AE activity of s-10-2 is relatively concentrated in the late loading stage, indicating that under a lower inclination, normal compaction and closure along the fissure plane dominate and interfacial sliding is partly suppressed. The AE activity of s-15-2 appears earlier, suggesting stronger coupling between the stress

concentration around the hole and the disturbance near the fissure tip. The cumulative ringing count of s-20-2 is relatively high, indicating that as the fissure inclination increases, the tangential component and interfacial sliding along the fissure plane are enhanced. Consequently, shear dislocation, local debonding, and secondary crack propagation are more likely to occur in the filling layer and at the rock-filling interface, leading to a more active AE response.

In summary, filled-fissure thickness mainly affects AE activity by changing the weak-interlayer range and the degree of interfacial deformation incompatibility, whereas fissure inclination mainly affects damage evolution by adjusting the relative proportions of normal compaction and tangential sliding along the weak interlayer. The former is mainly manifested by enhanced interfacial damage and sustained AE activity, while the latter is more closely related to changes in crack propagation paths and tensile-shear mixed failure.

### 3.4 Crack-type identification based on RA-AF parameters

To further distinguish the dominant fracture type during crack propagation under different filled-fissure configurations, RA-AF parameters were introduced based on the ringing count analysis to examine the tensile-shear failure characteristics during loading. The RA value is defined as the ratio of the AE signal rise time to amplitude, and the AF value is defined as the ratio of counts to duration:

$$AF=\frac{\text{Counts}}{\text{Duration}}\ (\text{kHz}) \tag{1}$$

$$RA=\frac{\text{Risetime}}{\text{Amplitude}}\ (\text{ms/V}) \tag{2}$$

During rock crack evolution, different crack modes have significant effects on crack morphology and structure. The average frequency (AF) and the ratio of rise time to amplitude (RA) in AE signals can be used to classify tensile and shear cracks in fissured rock masses. This method has been widely applied to crack identification in brittle material tests [42-45].

Tensile cracks mainly generate AE signals in the form of longitudinal waves with high energy, large amplitude, and short rise time, whereas shear cracks generate AE signals with longer duration and rise time, lower amplitude, and lower frequency. In AE waveforms, tensile cracks are characterized by higher AF and lower RA values; conversely, shear cracks are characterized by lower AF and higher RA values. Therefore, the fracture mode can be determined from the RA-AF scatter diagram, as shown in Fig. 11. The AF and RA values are plotted on the vertical and horizontal axes, respectively, and the graph is divided into upper and lower parts by a diagonal line passing through the origin. Points in the upper region correspond to tensile cracks, whereas points in the lower region correspond to shear microcracks.

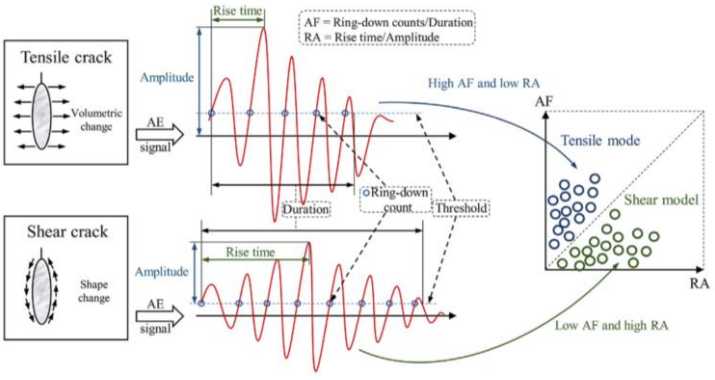



**Fig.11 Schematic diagram for identifying fracture modes based on RA-AF[45]**

Figures 12 and 13 show the normalized AF and RA values. The ratio of AF to RA is used to identify the crack type. Specifically, AF/RA > 1 indicates a tensile crack, whereas AF/RA < 1 indicates a shear crack. The results show that the tensile crack proportions of the intact and single-hole specimens are 98.4% and 97.2%, respectively, indicating that under low lateral confinement, microcrack propagation is dominated by tensile cracks. In the single-hole specimen, the hole edge is a typical stress concentration region and preferentially induces wing cracks around the hole and matrix splitting cracks;

thus, tensile cracks remain overwhelmingly dominant. Previous studies have shown that in sandstone containing holes, initial cracks mostly initiate at the upper and lower edges of the hole and then gradually propagate and coalesce, indicating that the hole strongly controls the crack initiation position and propagation path [5,6].

When the fissure thickness is maintained at 2 mm, the shear-type AE event proportions of s-10-2, s-15-2, and s-20-2 are 9.8%, 8.7%, and 21.0%, respectively. The shear event proportions of s-10-2 and s-15-2 are relatively similar, suggesting that within the low-inclination range of 10°-15°, a thin filled fissure is still dominated by compaction closure and local tensile propagation. When the fissure inclination increases to 20°, the proportion of shear-type events increases markedly, indicating that tangential sliding along the fissure plane, frictional dislocation at the rock-filling interface, and tensile-shear mixed propagation near the fissure tip are enhanced. The failure type of the specimen therefore changes from tensile-dominated to tensile-shear mixed failure. This result is consistent with the enhanced AE activity of the s-20-2 specimen shown in Fig. 10.

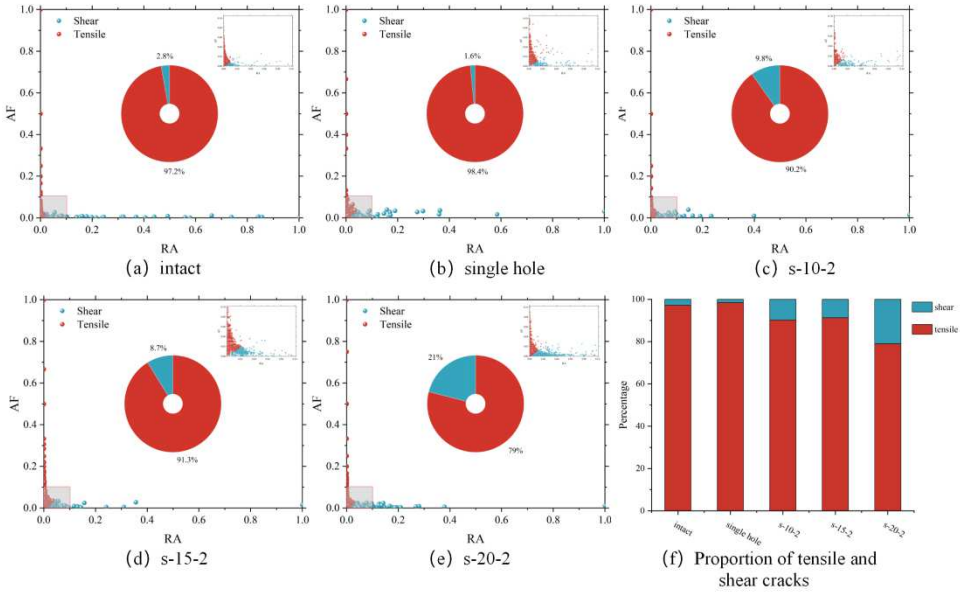



**Fig. 12 Classification Results of Crack Types Based on RA–AF Parameters for Specimens with Different Weak Interlayer Inclinations**

When the fissure inclination is kept at 15°, increasing the fissure thickness from 2 mm to 5 mm and 10 mm raises the shear-type AE event proportions to 67.5% and 63.9%, respectively, and the crack type changes from tensile-dominated to shear-dominated. This is because a thicker filling layer weakens the continuous load-bearing capacity between sandstone matrix blocks and increases the deformation incompatibility between the filling material and sandstone. As a result, compaction, debonding, frictional sliding, and shear dislocation are more likely to occur at the rock-filling interface. Under these conditions, the through-going filled fissure is no longer merely a local geometric defect but gradually becomes the dominant weak plane controlling the failure path, leading to a significant increase in shear-type AE events characterized by high RA and low AF values in the RA-AF diagram.

It should be noted that the shear-type event proportion of s-15-10 is slightly lower than that of s-15-5, although both are much higher than that of s-15-2. This indicates that increasing fissure thickness significantly enhances the tendency toward shear failure, while the difference between 5 mm and 10 mm may be related to the compaction degree of the filling layer, the interfacial contact state, and the reversal of local deformation direction. This also suggests that the influence of fissure thickness on the failure mechanism is not simply linearly enhanced, but is jointly controlled by filling-layer compaction and weak-interface sliding instability.

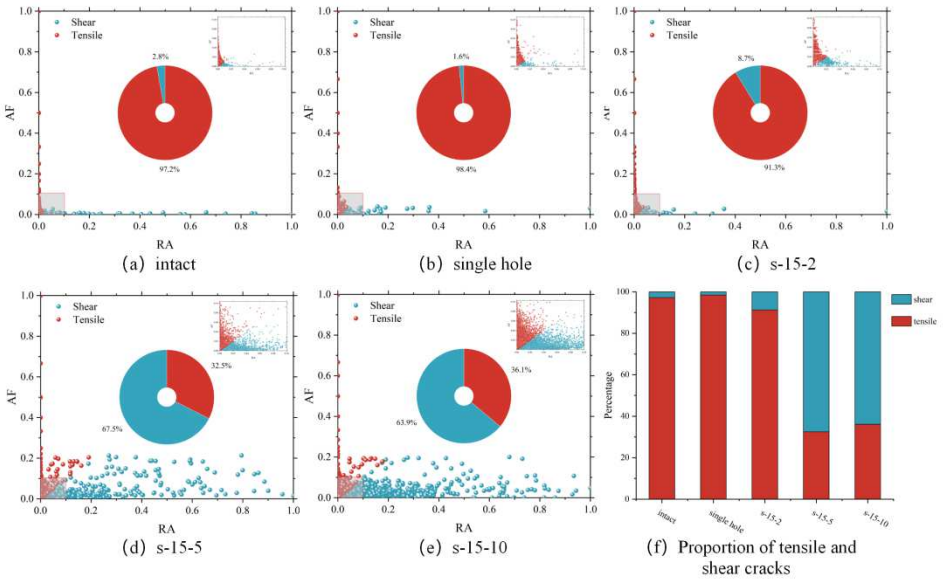



**Fig. 13 Classification Results of Crack Types Based on RA–AF Parameters for Specimens with Different Weak Interlayer Thicknesses**

Overall, the RA-AF classification results indicate that the hole mainly controls the initial crack initiation position, making tensile cracks around the hole the dominant failure form when transitioning from the intact specimen to the single-hole specimen. A thin through-going filled fissure mainly changes the crack propagation path and enhances local tensile-shear mixed effects. A thicker through-going filled fissure significantly enhances the controlling effect of the weak interlayer and interfacial shear sliding, causing the failure mechanism to change from tensile-dominated to shear-dominated. Combining the stress-strain curves, local deformation at the cavity roof, and AE ringing count results, the failure process of sandstone containing a circular hole and through-going filled fissure is controlled jointly by hole-induced stress concentration, compaction of the weak interlayer, interfacial sliding, and damage coalescence in the hole-fissure rock-bridge area.

**Table 4 Proportions of tensile and shear AE events based on RA-AF analysis**

| Specimen ID | Tensile event proportion (%) | Shear event proportion (%) | Dominant crack type |
|---|---|---|---|
| Intact specimen | 98.4 | 1.6 | Tensile-dominated |
| Single-hole specimen | 97.2 | 2.8 | Tensile-dominated |
| s-10-2 | 90.2 | 9.8 | Tensile-dominated |
| s-15-2 | 91.3 | 8.7 | Tensile-dominated |
| s-20-2 | 79.0 | 21.0 | Tensile-shear mixed |
| s-15-5 | 32.5 | 67.5 | Shear-dominated |
| s-15-10 | 36.1 | 63.9 | Shear-dominated |

## 4. Conclusions

(1) The intact specimen exhibited a peak strength of 80.01 MPa and a peak axial displacement of 2.48 mm. For the single-opening specimen, these values were 59.45 MPa and 1.89 mm, corresponding to reductions of 25.70% and 23.79%, respectively. All tested opening–fissure specimens exhibited lower peak strengths than the single-opening specimen.

(2) At a fixed fissure inclination of 15°, the measured peak strengths of s-15-2, s-15-5, and s-15-10 were 43.16, 48.96, and 47.90 MPa, respectively, while their peak axial displacements were 1.91, 1.93, and 2.16 mm. Within the three tested conditions, the peak strength increased from a filling thickness of 2 mm to 5 mm and then decreased slightly at 10 mm, whereas the peak axial displacement increased.

(3) At a fixed filling thickness of 2 mm, the measured peak strengths of s-10-2, s-15-2, and s-20-2 were 53.47, 43.16, and 55.61 MPa, respectively. Their peak axial displacements were 2.16, 1.91, and 3.73 mm. Among these specimens, s-15-2 exhibited the lowest peak strength, whereas s-20-2 exhibited the largest peak axial displacement.

(4) The measured peak local deformation at the opening roof was larger than that at the floor for all tested opening–fissure specimens. Specimen s-15-2 recorded the largest local deformation at both monitoring positions and the earliest recorded local instability times, showing the most pronounced local deformation concentration under the adopted loading path. Specimen s-15-5 recorded the latest roof local instability time and a relatively small floor deformation in its individual test.

(5) Specimens s-15-5 and s-15-10 exhibited more sustained AE activity during the middle and late loading stages than s-15-2. Based on the adopted RA–AF criterion, the proportions of AE hits classified as shear-type were 67.5% and 63.9% for s-15-5 and s-15-10, respectively. At a filling thickness of 2 mm, the corresponding proportions were 9.8%, 8.7%, and 21.0% for s-10-2, s-15-2, and s-20-2.

**Declarations**

**Fundings**

Not Applicable

**Consent to Publish**

Not applicable

**Ethics approval and consent to participate**

Not applicable

**Data Availability Statement**

The datasets generated during and/or analysed during the current study are not publicly available due to [the fact that they are part of an ongoing larger research project with subsequent unpublished studies, and the raw experimental data have not yet been systematically organized or standardized] but are available from the corresponding author on reasonable request.

# References

Chen, M.L., Jing, H.W., Ma, X.J., Su, H.J., Du, M.R., Zhu, T.T. (2017). Fracture evolution characteristics of sandstone containing double fissures and a single circular hole under uniaxial compression. Int. J. Min. Sci. Technol. 27, 499–505. http://doi.org/10.1016/j.ijmst.2017.03.027

Dong, Z., Cai, M., Ma, C., Wang, P., Li, P. (2024). Rock damage and fracture characteristics considering the interaction between holes and joints. Theor. Appl. Fract. Mech. 133, 104628. http://doi.org/10.1016/j.tafmec.2024.104628

Du, K., Liu, M., Yang, C., Tao, M., Feng, F., Wang, S. (2021). Mechanical and acoustic emission characteristics of rocks under biaxial confinements. Appl. Sci. 11, 769. http://doi.org/10.3390/app11020769

Huang, Y.H., Yang, S.Q., Tian, W.L., Zeng, W., Yu, L.Y. (2016). An experimental study on fracture mechanical behavior of rock-like materials containing two unparallel fissures under uniaxial compression. Acta Mech. Sin. 32, 442–455. http://doi.org/10.1007/s10409-015-0489-3

Ji, P.X., Viegas, G., Zhang, Q.B. (2024). Mechanical and fracturing characteristics of defected rock-like materials under biaxial compression. Int. J. Rock Mech. Min. Sci. 176, 105692. http://doi.org/10.1016/j.ijrmms.2024.105692

Jiang, X.Y., Wu, D., Zhao, Z.X., Yang, Y., Tian, J.W., Wang, F.L. (2024). Experimental and numerical study on the damage evolution and acoustic emission multi-parameter responses of single flaw sandstone under uniaxial compression. Theor. Appl. Fract. Mech. 133, 104535. http://doi.org/10.1016/j.tafmec.2024.104535

Le, H.L., Wei, J.H., Sun, S.R., Wang, W.C., Fan, H.T. (2021). Mechanical properties and cracking behaviors of limestone-like samples with two parallel fissures before and after grouting. J. Cent. South Univ. 28, 2875–2889.

http://doi.org/10.1007/s11771-021-4813-8

Lei, R.D., Zhang, Z.Y., Berto, F., Ranjith, P.G., Liu, L. (2020). Cracking process and acoustic emission characteristics of sandstone with two parallel filled-flaws under biaxial compression. Eng. Fract. Mech. 237, 107253. http://doi.org/10.1016/j.engfracmech.2020.107253

Li, B.L., Jiang, J.Y., Long, Y., Lin, Y., Jiang, M. (2026). True-triaxial deformation, cracking and strength failure characteristics of chemically corroded flawed sandstone. Bull. Eng. Geol. Environ. 85, 472. http://doi.org/10.1007/s10064-026-05093-w

Liu, B., Liu, Y., Xiao, P., Zhang, L. (2025). Effects of a single flaw on failure and acoustic emission characteristics around circular opening subjected to biaxial compression. Eng. Fail. Anal. 167, 109008. http://doi.org/10.1016/j.engfailanal.2024.109008

Li, N., Feng, Q., Yue, W., Sun, S., Li, Y., Li, G., Shi, W. (2023). Experimental study on mechanical and acoustic emission characteristics of sedimentary sandstone under different loading rates. Front. Earth Sci. 11, 1224645. http://doi.org/10.3389/feart.2023.1224645

Li, P., Cai, M.F., Wang, P.T., Guo, Q.F., Miao, S.J., Ren, F.H. (2021). Mechanical properties and energy evolution of jointed rock specimens containing an opening under uniaxial loading. Int. J. Miner. Metall. Mater. 28, 1875–1886. http://doi.org/10.1007/s12613-020-2237-3

Li, P., Cai, M.F., Gao, Y.B., Gorjian, M., Miao, S.J., Wang, Y. (2022). Macro/mesofracture and instability behaviors of jointed rocks containing a cavity under uniaxial compression using AE and DIC techniques. Theor. Appl. Fract. Mech. 122, 103620. http://doi.org/10.1016/j.tafmec.2022.103620

Liu, C., Yin, S.Y., Zhang, J., Zhang, D.M., Wang, L., Zhao, H.G. (2022). Acoustic emission and energy evolution laws of sandstone failure under deep mining-induced stress conditions. J. Min. Saf. Eng. 39, 470–479. http://doi.org/10.13545/j.cnki.jmse.2020.0643

Liu, J.P., Li, Y.H., Xu, S.D., Xu, S., Jin, C.Y., Liu, Z.S. (2015). Moment tensor analysis of acoustic emission for cracking mechanisms in rock with a pre-cut circular hole under uniaxial compression. Eng. Fract. Mech. 135, 206–218. http://doi.org/10.1016/j.engfracmech.2015.01.006

Liu, Q., Pan, C., Yan, L., Wang, X.G., Li, S.J., Cao, J.C. (2025). Acoustic emission characteristics and damage constitutive model of fractured sandstone under uniaxial compression. Sci. Rep. 15, 3128. http://doi.org/10.1038/s41598-025-85257-y

Liu, T., Wang, G., Wang, C., Wu, X., Chen, J., Zhang, H., Chen, H., Zheng, C. (2025). Experimental study on mechanical and acoustic emission characteristics of red sandstone containing combined flaws of hole–fissure under biaxial compression. Can. Geotech. J. 62, 1–16. http://doi.org/10.1139/cgj-2024-0179

Liu, X.R., Yang, S.Q., Huang, Y.H., Cheng, J.L. (2019). Experimental study on the strength and fracture mechanism of sandstone containing elliptical holes and fissures under uniaxial compression. Eng. Fract. Mech. 205, 205–217. http://doi.org/10.1016/j.engfracmech.2018.11.028

Miao, S.J., Shang, X.F., Chang, N.D., Ma, Y.K., Yang, P.J. (2025). Mechanical properties and fracture mechanism of porous sandstone under biaxial compression. J. Min. Strata Control Eng. 7, 023041. http://doi.org/10.13532/j.jmsce.cn10-1638/td.2025-1048

Miao, S.T., Pan, P.Z., Wu, Z.H., Li, S.J., Zhao, S.K. (2018). Fracture analysis of sandstone with a single filled flaw under uniaxial compression. Eng. Fract. Mech. 204, 319–343. http://doi.org/10.1016/j.engfracmech.2018.10.009

Niu, Y., Zhou, X.P., Berto, F. (2020). Evaluation of fracture mode classification in flawed red sandstone under uniaxial compression. Theor. Appl. Fract. Mech. 107, 102528. http://doi.org/10.1016/j.tafmec.2020.102528

Ohno, K., Ohtsu, M. (2010). Crack classification in concrete based on acoustic emission. Constr. Build. Mater. 24, 2339–2346. http://doi.org/10.1016/j.conbuildmat.2010.05.004

Peng, K., Lai, R.Z., Luo, S., Li, X.B. (2024). Influence of axial stress on failure characteristics of deep arched hard rock

roadway. Trans. Nonferrous Met. Soc. China 34, 4032–4048. http://doi.org/10.1016/S1003-6326(24)66656-2

Qin, T., Sun, H., Liu, H., Zhang, J., Li, T., Liu, G., Liu, Z. (2018). Experimental study on mechanical and acoustic emission characteristics of rock samples under different stress paths. Shock Vib. 2018, 4813724. http://doi.org/10.1155/2018/4813724

Sharafisafa, M., Shen, L.M., Zheng, Y.G., Xiao, J.Z. (2019). The effect of flaw filling material on the compressive behaviour of 3D printed rock-like discs. Int. J. Rock Mech. Min. Sci. 117, 105–117. http://doi.org/10.1016/j.ijrmms.2019.03.031

Su, H.J., Zhang, L.Q., Wu, C., Chen, G.F., Zhang, B.Y. (2025). Fracture characteristics and deformation evolution of sandstone in grout-reinforced holes. J. Min. Strata Control Eng. 7, 033042. http://doi.org/10.13532/j.jmsce.cn10-1638/td.2024-1382

Wang, Z., Lin, H., Feng, X., Yang, C., Ou, K., Chen, Y. (2025). Fracture characteristics and damage mechanisms of heat-treated sandstone with combined hole-joint flaws under uniaxial compression. Theor. Appl. Fract. Mech. 136, 104845. http://doi.org/10.1016/j.tafmec.2025.104845

Wang, H., Fall, M., Miao, S. (2024). Characteristics of fracture changes and fatigue failure signals for siltstone under cyclic loading. Int. J. Rock Mech. Min. Sci. 174, 105645. http://doi.org/10.1016/j.ijrmms.2024.105645

Wang, J.X., Liang, P., Zhang, Y.B., Yao, X.L., Yu, G.Y., Guo, B. (2024). Research on classification of rock tensile-shear fracture based on acoustic emission RA-AF values and Kneedle algorithm. Chin. J. Rock Mech. Eng. 43, 3267–3279. http://doi.org/10.13722/j.cnki.jrme.2023.0696

Wang, W., Sun, S., Le, H., Shu, Y., Zhu, F., Fan, H., Liu, Y. (2019). Experimental and numerical study on failure modes and shear strength parameters of rock-like specimens containing two infilled flaws. Int. J. Civ. Eng. 17, 1895–1908. http://doi.org/10.1007/s40999-019-00449-8

Wong, L.N.Y., Einstein, H.H. (2009). Systematic evaluation of cracking behavior in specimens containing single flaws under uniaxial compression. Int. J. Rock Mech. Min. Sci. 46, 239–249. http://doi.org/10.1016/j.ijrmms.2008.03.006

Xue, K.S., Pu, H., Lu, Y.L., Chen, Y.L., Wu, Y., Li, M., Liu, D.J., Xu, J.C. (2026). Crack type classification of fissured sandstone using acoustic emission and Gaussian mixture modeling: Effects of fissure inclination angles. J. Cent. South Univ. 33, 2166–2188. http://doi.org/10.1007/s11771-026-6292-4

Yu, X., Zuo, J.P., Mao, L., Li, Y., Yang, L. (2024). Crack propagation behavior and failure prediction of rocks with non-parallel conjugate flaws: Insights from the perspective of acoustic emission and DIC. Theor. Appl. Fract. Mech. 134, 104709. http://doi.org/10.1016/j.tafmec.2024.104709

Yang, S.Q., Jing, H.W., Xu, T. (2014). Mechanical behavior and failure analysis of brittle sandstone specimens containing combined flaws under uniaxial compression. J. Cent. South Univ. 21, 2059–2073. http://doi.org/10.1007/s11771-014-2155-5

Yang, S.Q., Huang, Y.H., Tian, W.L., Zhu, J.B. (2017). An experimental investigation on strength, deformation and crack evolution behavior of sandstone containing two oval flaws under uniaxial compression. Eng. Geol. 217, 35–48. http://doi.org/10.1016/j.enggeo.2016.12.004

Yang, S.Q., Yin, P.F., Chen, M., Zhou, X.P., Jing, H.W., Zhang, Q.Y. (2019). Failure behavior and crack evolution mechanism of a non-persistent jointed rock mass containing a circular hole. Int. J. Rock Mech. Min. Sci. 114, 101–121. http://doi.org/10.1016/j.ijrmms.2018.12.017

Zhang, J.Z., Zhou, X.P., Du, Y.H. (2023). Cracking behaviors and acoustic emission characteristics in brittle failure of flawed sandstone: A true triaxial experiment investigation. Rock Mech. Rock Eng. 56, 167–182. http://doi.org/10.1007/s00603-022-03087-0

Zhao, N., Ding, M.R., Wei, S., Wang, L.G. (2026). Study on acoustic emission response and damage evolution characteristics of sandstone with X-shaped fissures at different inclination angles under uniaxial compression. Geomech. Geophys. Geo-Energy Geo-Resour. (online first). http://doi.org/10.1007/s40948-026-01170-2

Zhao, F., Shi, Z.M., Yu, S.B., Zheng, H.C. (2023). A review of fracture mechanic behaviors of rocks containing various defects. Underground Space 12, 102–115. http://doi.org/10.1016/j.undsp.2023.02.006

Zhao, Y., Li, X., Huang, L., Zhang, Z., Xu, Z. (2024). Characteristic stress variation and microcrack evolution of granite subjected to uniaxial compression using acoustic emission methods. J. Rock Mech. Geotech. Eng. 16, 3511–3523. http://doi.org/10.1016/j.jrmge.2023.11.023

Zhou, X., Zhang, D.M., Nowamooz, H., Ye, C. (2024). Failure and acoustic behavior of combinational flaws sandstone subjected to dynamic compression loads. Theor. Appl. Fract. Mech. 129, 104169. http://doi.org/10.1016/j.tafmec.2023.104169

Zhu, Q.Q., Li, D.Y., Han, Z.Y., Li, X.B., Zhou, Z.L. (2019). Mechanical properties and fracture evolution of sandstone specimens containing different inclusions under uniaxial compression. Int. J. Rock Mech. Min. Sci. 115, 33–47. http://doi.org/10.1016/j.ijrmms.2019.01.010

Zhu, T.T., Jing, H.W., Su, H.J., Yin, Q., Du, M.R. (2015). Mechanical behavior of sandstone containing double circular cavities under uniaxial compression. Chin. J. Geotech. Eng. 37, 1047–1056. http://doi.org/10.11779/CJGE201506011

Zhuang, X., Chun, J., Zhu, H. (2014). A comparative study on unfilled and filled crack propagation for rock-like brittle material. Theor. Appl. Fract. Mech. 72, 110–120. http://doi.org/10.1016/j.tafmec.2014.04.004